The Astrophysical Journal, 965:73 (14pp), 2024 April 10 https://doi.org/10.3847/1538-4357/ad2618

SN 2020udy: A New Piece of the Homogeneous Bright Group in the Diverse Iax Subclass

Mridweeka Singh[1], Devendra K. Sahu[1], Barnabás Barna[2], Anjasha Gangopadhyay[3], Raya Dastidar[4,5], Rishabh Singh Teja[1,6], Kuntal Misra[7], D. Andrew Howell[8,9], Xiaofeng Wang[10,11], Jun Mo[10], Shengyu Yan[10], Daichi Hiramatsu[8,9,12,13], Craig Pellegrino[8,9], G. C. Anupama[1], Arti Joshi[14], K. Azalee Bostroem[15], Jamison Burke[8,9], Curtis McCully[8,9], Rama Subramanian V[16], Gaici Li[10], Gaobo Xi[10], Xin Li[11], Zhitong Li[17], Shubham Srivastav[18], Hyobin Im[19,20], and Anirban Dutta[1,21]

[1] Indian Institute of Astrophysics, Koramangala 2nd Block, Bangalore 560034, India; mridweeka.singh@iiap.res.in, yashasvi04@gmail.com
[2] Department of Experimental Physics, Institute of Physics, University of Szeged, H-6720 Szeged, Dóm tér 9, Hungary
[3] Hiroshima Astrophysical Science Center, Hiroshima University, Higashi-Hiroshima, Japan
[4] Millennium Institute of Astrophysics (MAS), Nuncio Monsenor Sòtero Sanz 100, Providencia, Santiago RM, Chile
[5] Instituto de Astrofísica, Universidad Andres Bello, Fernandez Concha 700, Las Condes, Santiago RM, Chile
[6] Pondicherry University, R.V. Nagar, Kalapet, 605014, Puducherry, India
[7] Aryabhatta Research Institute of observational sciencES, Manora Peak, Nainital, 263001, India
[8] Las Cumbres Observatory, 6740 Cortona Drive, Suite 102, Goleta, CA 93117-5575, USA
[9] Department of Physics, University of California, Santa Barbara, CA 93106-9530, USA
[10] Physics Department, Tsinghua University, Beijing, 100084, People's Republic of China
[11] Beijing Planetarium, Beijing Academy of Science and Technology, Beijing, 100044, People's Republic of China
[12] Center for Astrophysics | Harvard & Smithsonian, 60 Garden Street, Cambridge, MA 02138-1516, USA
[13] The NSF AI Institute for Artificial Intelligence and Fundamental Interactions, USA
[14] Institute of Astrophysics, Pontificia Universidad Católica de Chile, Av. Vicuña MacKenna 4860, 7820436, Santiago, Chile
[15] DiRAC Institute, Department of Astronomy, University of Washington, Box 351580, U.W., Seattle, WA 98195, USA
[16] Department of Sciences, Amrita School of Physical Sciences, Amrita Vishwa Vidyapeetham, Coimbatore, Tamil Nadu, 641112, India
[17] National Astronomical Observatories of China, Chinese Academy of Sciences, Beijing, 100012, People's Republic of China
[18] Astrophysics Research Centre, School of Mathematics and Physics, Queen's University Belfast, Belfast BT7 1NN, UK
[19] Korea Astronomy and Space Science Institute, 776 Daedeokdae-ro, Yuseong-gu, Daejeon 34055, Republic of Korea
[20] Korea University of Science and Technology (UST), 217 Gajeong-ro, Yuseong-gu, Daejeon 34113, Republic of Korea
[21] Pondicherry University, Chinna Kalapet, Kalapet, Puducherry 605014, India
Received 2023 August 31; revised 2023 December 27; accepted 2024 January 12; published 2024 April 8

Abstract

We present optical observations and analysis of the bright type Iax supernova SN 2020udy hosted by NGC 0812. The evolution of the light curve of SN 2020udy is similar to that of other bright type Iax SNe. Analytical modeling of the quasi-bolometric light curves of SN 2020udy suggests that 0.08 ± 0.01 $M_{\odot}$ of ^{56}Ni would have been synthesized during the explosion. The spectral features of SN 2020udy are similar to those of the bright members of type Iax class, showing a weak Si II line. The late-time spectral sequence is mostly dominated by iron group elements with broad emission lines. Abundance tomography modeling of the spectral time series of SN 2020udy using TARDIS indicates stratification in the outer ejecta; however, to confirm this, spectral modeling at a very early phase is required. After maximum light, uniform mixing of chemical elements is sufficient to explain the spectral evolution. Unlike in the case of normal type Ia SNe, the photospheric approximation remains robust until +100 days, requiring an additional continuum source. Overall, the observational features of SN 2020udy are consistent with the deflagration of a carbon–oxygen white dwarf.

Unified Astronomy Thesaurus concepts: Supernovae (1668)

Supporting material: data behind figure, machine-readable table

1. Introduction

Thermonuclear supernovae (SNe), also known as type Ia SNe, are the outcome of the explosive burning of carbon–oxygen (CO) white dwarfs. They are known as a one-parameter family and are extensively used in cosmology as standard candles (Phillips 1993; Phillips et al. 1999). With the increasing sample size, diversity has been observed among type Ia SNe, leading to their subclassification (Taubenberger 2017). Distinguishing different subclasses can help improve the precision of their distance measurements (Wang et al. 2009) and identify their physical origins (Wang et al. 2013).

There are different subtypes of type Ia SNe that have some similarities and dissimilarities. Among them, type Iax SNe (Li et al. 2003; Jha et al. 2006b; Foley et al. 2013) are one of the peculiar subclasses, having low luminosity ($M_r = -12.7$ mag, Karambelkar et al. 2021, to $M_V = -18.4$ mag, Narayan et al. 2011) and a lower energy budget (Jha 2017, and references therein). The light curves of SNe Iax are characterized by a faster rise to the maximum and post-maximum decline in the bluer bands than normal type Ia SNe (Magee et al. 2016, 2017; Jha 2017; Li et al. 2018). Due to the lack of fairly good pre-maximum coverage for a good fraction of type Iax SNe, precise measurement of peak absolute magnitudes and rise time is difficult. This also poses a problem in putting strong observational constraints on the explosion models. The occurrence rate of SNe Iax is ∼5%–30% of that of normal type Ia SNe (Foley et al. 2013; Miller et al. 2017; Srivastav et al. 2022).

Table 1
Optical Photometric Measurements of SN 2020udy

Date	JD[a]	Phase[b] (days)	B (mag)	g (mag)	V (mag)	r (mag)	i (mag)	Telescope[c]
2020-09-29	122.24	−8.29	17.27 ± 0.02	17.16 ± 0.01	17.27 ± 0.02	17.17 ± 0.01	17.34 ± 0.02	2
2020-10-01	124.23	−6.30	16.91 ± 0.03	16.82 ± 0.01	16.92 ± 0.02	16.85 ± 0.01	17.02 ± 0.01	2
2020-10-02	124.98	−5.55	16.80 ± 0.04	16.78 ± 0.05	16.70 ± 0.03	16.72 ± 0.03	16.94 ± 0.07	1
2020-10-04	127.19	−3.34	16.80 ± 0.02	16.58 ± 0.01	16.66 ± 0.02	16.57 ± 0.00	16.69 ± 0.01	2
2020-10-05	127.98	−2.55	16.56 ± 0.03	16.61 ± 0.04	16.42 ± 0.03	16.34 ± 0.04	16.49 ± 0.05	1
2020-10-05	128.23	−2.30	16.74 ± 0.01	16.55 ± 0.00	16.57 ± 0.01	16.48 ± 0.01	16.61 ± 0.01	2
2020-10-07	130.18	−0.35	16.72 ± 0.01	16.46 ± 0.00	16.41 ± 0.01	16.35 ± 0.00	16.47 ± 0.01	2
2020-10-08	130.88	0.35	16.49 ± 0.09	16.46 ± 0.13	16.10 ± 0.16	16.28 ± 0.04	⋯	1
2020-10-11	133.73	3.20	16.74 ± 0.05	16.55 ± 0.06	16.23 ± 0.11	16.18 ± 0.03	16.30 ± 0.04	1
2020-10-16	139.23	8.70	17.38 ± 0.01	16.86 ± 0.00	16.45 ± 0.00	16.21 ± 0.00	16.25 ± 0.00	2
2020-10-17	139.63	9.10	17.39 ± 0.03	16.99 ± 0.03	16.45 ± 0.02	16.20 ± 0.04	16.19 ± 0.03	1
2020-10-17	140.22	9.69	17.47 ± 0.02	16.93 ± 0.01	16.48 ± 0.01	16.23 ± 0.01	16.22 ± 0.01	2
2020-10-18	141.19	10.66	17.63 ± 0.01	17.04 ± 0.01	16.53 ± 0.01	16.26 ± 0.00	16.24 ± 0.01	2
2020-10-19	142.23	11.70	17.74 ± 0.02	17.13 ± 0.01	16.59 ± 0.01	16.28 ± 0.00	16.24 ± 0.01	2
2020-10-20	142.77	12.24	17.77 ± 0.09	17.40 ± 0.05	16.70 ± 0.09	16.32 ± 0.05	16.22 ± 0.06	1
2020-10-21	144.21	13.68	18.03 ± 0.02	17.38 ± 0.01	16.75 ± 0.01	16.39 ± 0.00	16.31 ± 0.00	2
2020-10-22	144.94	14.41	18.06 ± 0.04	17.68 ± 0.06	16.84 ± 0.05	16.50 ± 0.10	16.33 ± 0.08	1
2020-10-22	144.94	14.41	18.10 ± 0.07	17.61 ± 0.05	16.86 ± 0.06	16.51 ± 0.09	16.31 ± 0.09	1
2020-10-23	146.33	15.80	18.29 ± 0.02	17.59 ± 0.00	16.92 ± 0.01	16.50 ± 0.00	16.40 ± 0.00	2
2020-10-25	148.29	17.76	18.51 ± 0.03	17.79 ± 0.01	17.05 ± 0.01	16.61 ± 0.01	16.48 ± 0.01	2
2020-10-26	149.28	18.75	18.52 ± 0.03	17.79 ± 0.01	17.12 ± 0.01	16.67 ± 0.00	16.49 ± 0.01	2
2020-10-31	153.90	23.37	18.98 ± 0.10	18.43 ± 0.06	17.38 ± 0.03	16.77 ± 0.05	16.56 ± 0.05	1
2020-10-31	153.91	23.38	19.03 ± 0.09	18.38 ± 0.06	17.48 ± 0.03	16.70 ± 0.06	⋯	1
2020-11-03	157.28	26.75	18.96 ± 0.11	18.34 ± 0.05	17.65 ± 0.04	17.18 ± 0.01	16.98 ± 0.02	2
2020-11-04	157.75	27.22	19.12 ± 0.06	18.40 ± 0.06	17.64 ± 0.03	17.03 ± 0.05	16.76 ± 0.05	1
2020-11-04	157.75	27.22	19.01 ± 0.05	18.40 ± 0.04	17.62 ± 0.04	17.03 ± 0.06	16.72 ± 0.06	1
2020-11-04	158.23	27.70	19.19 ± 0.11	18.36 ± 0.04	17.68 ± 0.03	17.14 ± 0.01	16.96 ± 0.01	2
2020-11-06	160.23	29.70	19.23 ± 0.09	18.47 ± 0.02	17.75 ± 0.02	17.27 ± 0.01	17.10 ± 0.01	2
2020-11-07	161.22	30.69	18.94 ± 0.08	18.38 ± 0.03	17.62 ± 0.03	17.25 ± 0.01	17.03 ± 0.02	2
2020-11-08	161.87	31.34	19.08 ± 0.13	18.52 ± 0.04	17.61 ± 0.02	17.19 ± 0.04	17.14 ± 0.01	1
2020-11-08	162.23	31.70	19.17 ± 0.05	18.50 ± 0.03	17.62 ± 0.02	17.21 ± 0.04	⋯	2
2020-11-08	162.24	31.71	⋯	⋯	17.79 ± 0.02	17.32 ± 0.01	⋯	2
2020-11-09	163.26	32.73	19.32 ± 0.04	18.55 ± 0.01	17.85 ± 0.01	17.40 ± 0.01	17.21 ± 0.01	2
2020-11-10	163.89	33.36	19.22 ± 0.03	18.63 ± 0.04	17.79 ± 0.01	17.33 ± 0.05	17.19 ± 0.06	1
2020-11-10	163.89	33.36	19.27 ± 0.04	18.65 ± 0.04	17.77 ± 0.02	⋯	17.09 ± 0.05	1
2020-11-13	167.26	36.73	19.40 ± 0.09	⋯	17.92 ± 0.02	⋯	⋯	2
2020-11-14	167.75	37.22	19.35 ± 0.05	18.75 ± 0.04	17.99 ± 0.04	⋯	17.37 ± 0.09	1
2020-11-14	167.76	37.23	19.34 ± 0.05	18.77 ± 0.04	17.98 ± 0.05	⋯	⋯	1
2020-11-15	169.21	38.68	19.34 ± 0.05	18.63 ± 0.02	17.97 ± 0.02	17.55 ± 0.01	17.40 ± 0.01	2
2020-11-18	171.76	41.23	19.22 ± 0.12	⋯	17.83 ± 0.08	⋯	⋯	1
2020-11-18	171.77	41.24	19.24 ± 0.08	⋯	17.89 ± 0.08	⋯	⋯	1
2020-11-22	175.84	45.31	⋯	18.70 ± 0.06	⋯	⋯	17.61 ± 0.05	1
2020-11-22	175.84	45.31	⋯	18.71 ± 0.06	⋯	⋯	17.71 ± 0.09	1
2020-11-26	179.81	49.28	19.44 ± 0.07	18.74 ± 0.08	17.95 ± 0.05	17.93 ± 0.13	17.72 ± 0.06	1
2020-11-26	179.82	49.29	⋯	⋯	17.87 ± 0.05	⋯	17.89 ± 0.06	1
2020-11-27	181.08	50.55	19.44 ± 0.26	18.62 ± 0.08	18.27 ± 0.07	17.88 ± 0.03	17.73 ± 0.03	2
2020-11-28	182.05	51.52	19.32 ± 0.17	⋯	18.23 ± 0.06	17.91 ± 0.03	17.75 ± 0.03	2
2020-11-29	183.02	52.49	19.54 ± 0.21	18.72 ± 0.09	18.19 ± 0.06	17.92 ± 0.04	17.80 ± 0.03	2
2020-11-30	184.14	53.61	19.46 ± 0.17	18.82 ± 0.07	18.18 ± 0.07	17.95 ± 0.03	17.78 ± 0.03	2
2020-12-02	185.71	55.18	19.53 ± 0.09	18.99 ± 0.06	18.22 ± 0.05	17.96 ± 0.06	17.82 ± 0.08	1
2020-12-02	185.72	55.19	19.52 ± 0.09	18.91 ± 0.06	18.29 ± 0.04	17.91 ± 0.06	17.89 ± 0.09	1
2020-12-02	186.07	55.54	19.92 ± 0.30	18.89 ± 0.11	18.10 ± 0.07	17.93 ± 0.04	17.87 ± 0.04	2
2020-12-03	187.09	56.56	19.48 ± 0.14	18.82 ± 0.05	18.32 ± 0.04	18.03 ± 0.02	17.92 ± 0.02	2
2020-12-04	188.09	57.56	19.57 ± 0.09	18.86 ± 0.04	18.28 ± 0.02	17.98 ± 0.01	17.89 ± 0.02	2
2020-12-08	191.71	61.18	19.49 ± 0.15	⋯	⋯	⋯	⋯	1
2020-12-09	193.02	62.49	19.55 ± 0.05	18.90 ± 0.02	18.38 ± 0.02	18.12 ± 0.01	18.02 ± 0.01	2
2020-12-10	194.05	63.52	19.64 ± 0.05	18.94 ± 0.02	18.45 ± 0.02	18.18 ± 0.01	18.04 ± 0.01	2
2020-12-11	195.05	64.52	19.73 ± 0.07	18.95 ± 0.02	18.45 ± 0.02	18.17 ± 0.01	18.07 ± 0.02	2
2020-12-12	195.70	65.17	19.71 ± 0.04	⋯	18.42 ± 0.10	⋯	⋯	1
2020-12-12	195.71	65.18	19.69 ± 0.03	⋯	18.44 ± 0.10	⋯	⋯	1
2020-12-16	200.11	69.58	19.68 ± 0.04	18.99 ± 0.02	18.53 ± 0.02	18.29 ± 0.01	18.20 ± 0.01	2
2020-12-17	201.09	70.56	19.53 ± 0.06	18.98 ± 0.03	18.51 ± 0.02	18.26 ± 0.02	18.17 ± 0.02	2
2020-12-18	201.76	71.23	19.61 ± 0.04	18.87 ± 0.06	18.44 ± 0.02	18.24 ± 0.08	18.10 ± 0.06	1

Table 1
(Continued)

Date	JD[a]	Phase[b] (days)	B (mag)	g (mag)	V (mag)	r (mag)	i (mag)	Telescope[c]
2020-12-18	201.78	71.25	19.61 ± 0.04	18.91 ± 0.05	18.47 ± 0.02	18.15 ± 0.08	⋯	1
2020-12-25	208.71	78.18	19.79 ± 0.07	18.97 ± 0.10	18.35 ± 0.05	⋯	⋯	1
2020-12-25	208.71	78.18	19.84 ± 0.07	18.97 ± 0.11	18.32 ± 0.05	⋯	⋯	1
2021-01-02	216.72	86.19	19.96 ± 0.08	19.24 ± 0.11	18.85 ± 0.04	18.61 ± 0.09	⋯	1
2021-01-02	216.72	86.19	19.93 ± 0.08	19.27 ± 0.11	18.84 ± 0.05	⋯	⋯	1
2021-01-08	222.70	92.17	19.90 ± 0.06	⋯	18.64 ± 0.04	⋯	⋯	1
2021-01-08	222.71	92.18	19.99 ± 0.06	⋯	18.69 ± 0.04	⋯	⋯	1
2021-01-12	227.03	96.50	⋯	19.25 ± 0.14	18.89 ± 0.19	18.73 ± 0.08	18.53 ± 0.07	2
2021-01-14	228.71	98.18	⋯	⋯	⋯	18.83 ± 0.05	⋯	2
2021-01-14	228.71	98.18	⋯	⋯	⋯	18.85 ± 0.05	⋯	2
2021-01-15	230.07	99.54	⋯	⋯	18.70 ± 0.06	18.50 ± 0.05	18.48 ± 0.04	2
2021-01-16	231.10	100.57	19.92 ± 0.08	19.21 ± 0.05	19.00 ± 0.05	18.95 ± 0.03	18.72 ± 0.03	2
2021-01-17	232.06	101.53	20.05 ± 0.09	19.37 ± 0.05	19.04 ± 0.04	18.95 ± 0.03	18.80 ± 0.03	2
2021-01-26	240.61	110.08	19.93 ± 0.15	⋯	18.95 ± 0.07	18.89 ± 0.10	⋯	1
2021-01-26	240.63	110.10	⋯	⋯	19.04 ± 0.12	18.89 ± 0.13	⋯	1
2021-01-30	245.04	114.51	⋯	19.22 ± 0.24	18.62 ± 0.31	19.03 ± 0.15	18.93 ± 0.14	2
2021-02-01	246.62	116.09	20.00 ± 0.21	19.67 ± 0.21	⋯	19.18 ± 0.11	⋯	1
2021-02-01	246.64	116.11	⋯	19.67 ± 0.25	⋯	19.17 ± 0.11	⋯	1
2021-02-04	250.04	119.51	19.67 ± 0.31	19.17 ± 0.31	18.93 ± 0.22	18.91 ± 0.18	18.90 ± 0.13	2
2021-02-07	252.62	122.09	20.40 ± 0.31	19.90 ± 0.29	19.28 ± 0.24	⋯	⋯	1

Notes.
[a] JD 2459000+.
[b] Phase has been calculated with respect to B_{max} on JD 2459130.53.
[c] 1: LCO, 2: TNT.

(This table is available in its entirety in machine-readable form.)

As a class, type Iax SNe show homogeneous spectral evolution (Jha et al. 2006a; Jha 2017) with low expansion velocities at maximum ranging from 2000 to 8000 km s^{-1} (Foley et al. 2009; Stritzinger et al. 2014). The early spectra of SNe Iax show Fe III features along with features due to intermediate-mass elements (IMEs), similar to 1991T-like SNe. During the late phase, type Iax SNe exhibit significant differences from the type Ia class. Strong and wide P-Cygni lines dominate the optical wavelengths until 4–6 months after explosion. Even later, type Iax SNe do not enter into a fully nebular phase. Permitted spectral lines mainly of Fe coexist with forbidden emission lines in the late-time spectra of all type Iax SNe (McCully et al. 2014a; Stritzinger et al. 2015; Foley et al. 2016). The spectral synthesis of SN 2014dt (the only example with continuous observations from its maximum to +550 days) showed that the assumption of an expanding photosphere provides a remarkable match with the observed spectral evolution during the first ∼100 days. At even later epochs, the approximation is capable of reproducing the P-Cygni lines formed by Fe, Ca, and Na (Camacho-Neves et al. 2023).

The progenitor system and explosion scenario of type Iax SNe has been a matter of debate for many years. Being low-luminosity and less energetic events, type Iax SNe hint toward a different progenitor scenario from type Ia SNe. High-resolution pre-explosion images of a few type Iax SNe, obtained with the Hubble Space Telescope, are used to identify the progenitor systems of these events. SN 2012Z is one such type Iax SNe, hosted by the nearby galaxy NGC 1309. McCully et al. (2014b) analyzed the pre-explosion images of SN 2012Z and suggested that a binary consisting of a white dwarf and a helium star is one of the most plausible progenitor systems for this SN. Another type Iax with pre-explosion images is SN 2014dt, and a similar progenitor system has been suggested as one of the possibilities (Foley et al. 2015) for this SN. However, except for a few type Iax SNe (Foley et al. 2013; Greiner et al. 2023), helium is not detected in spectroscopic

Table 2
Log of Spectroscopic Observations of SN 2020udy

Date	JD[a]	Phase[b] (days)	Spectral Range (Å)	Telescope/Instrument
2020-10-01	123.87	−6.6	3300–11000	FTN/FLOYDS
2020-10-02	125.20	−5.3	3500–10000	Xinglong/BFOSC
2020-10-04	127.19	−3.3	3500–10000	Xinglong/BFOSC
2020-10-07	129.82	−0.7	3300–11000	FTN/FLOYDS
2020-10-09	132.21	1.68	3500–10000	Xinglong/BFOSC
2020-10-15	137.81	7.27	3300–11000	FTN/FLOYDS
2020-10-19	142.15	11.6	3500–10000	Xinglong/BFOSC
2020-10-21	143.88	13.4	3300–11000	FTN/FLOYDS
2020-10-23	144.94	14.4	3500–9000	ARC/DIS
2020-10-26	148.81	18.3	3300–11000	FTN/FLOYDS
2020-10-26	149.17	18.6	3500–10000	Xinglong/BFOSC
2020-10-27	150.29	19.7	3500–10000	Xinglong/BFOSC
2020-11-04	157.87	27.3	3300–11000	FTN/FLOYDS
2020-11-13	166.76	36.2	3300–11000	FTN/FLOYDS
2020-11-14	168.20	37.7	3500–10000	Xinglong/BFOSC
2020-11-26	179.91	49.4	3300–11000	FTN/FLOYDS
2020-12-03	186.89	56.4	3300–11000	FTN/FLOYDS
2020-12-23	206.86	76.3	3300–11000	FTN/FLOYDS
2021-01-05	219.81	89.3	3300–11000	FTN/FLOYDS
2021-02-06	251.72	121.2	3300–11000	FTN/FLOYDS

Notes.
[a] JD 2459000+.
[b] Phase has been calculated with respect to B_{max} on JD 2459130.53.

Table 3
Light-curve Parameters of SN 2020udy

SN 2020udy	*B* band	*g* band	*V* band	*r* band	*i* band
JD of maximum light (2459000+)	130.53 ± 1.0	130.54 ± 1.0	130.54 ± 1.0	133.74 ± 1.0	139.93 ± 1.0
Magnitude at maximum (mag)	16.72 ± 0.02	16.46 ± 0.01	16.40 ± 0.01	16.18 ± 0.03	16.25 ± 0.01
Absolute magnitude at maximum (mag)	−17.41 ± 0.34	−17.56 ± 0.34	−17.76 ± 0.34	−17.83 ± 0.34	−17.82 ± 0.33
Δm_{15} (mag)	1.36 ± 0.04	1.18 ± 0.04	0.45 ± 0.04	0.49 ± 0.03	0.66 ± 0.04

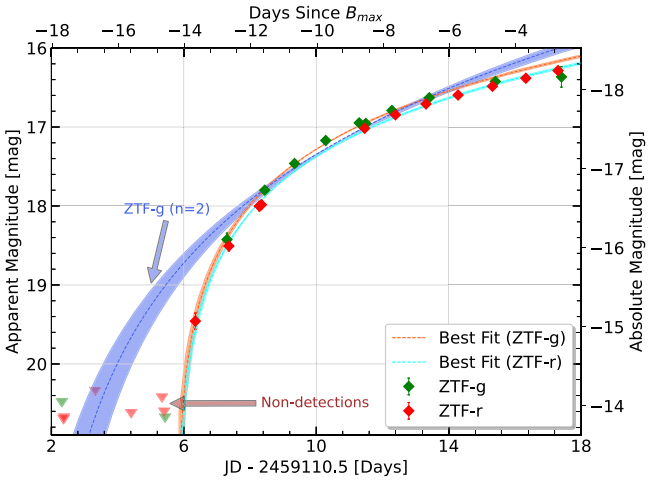

Figure 1. Estimation of explosion epoch using an analytical expression for the early rise. The 1σ deviations around the best fits are shown with the shaded regions.

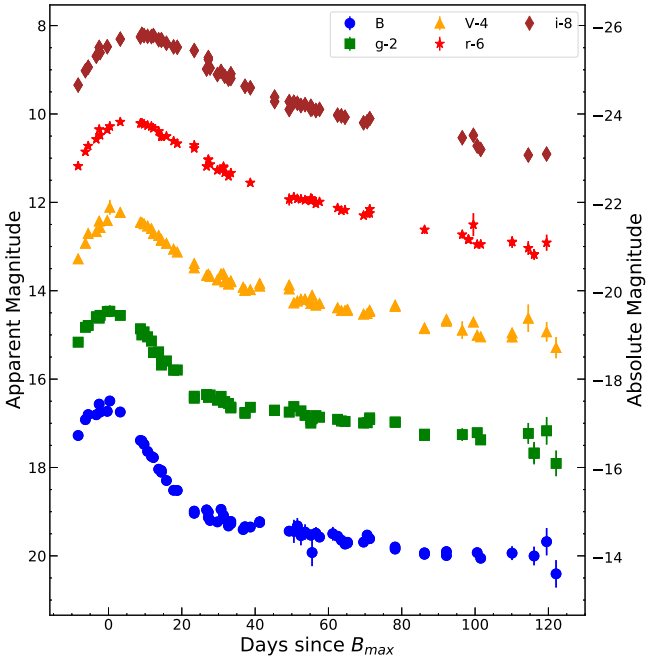

Figure 2. Evolution of the light curve of SN 2020udy in the *BgVri* bands.

studies (White et al. 2015; Jacobson-Galán et al. 2019; Magee et al. 2019).

The observed explosion parameters of many of the bright type Iax SNe are successfully explained by the pure deflagration of a CO white dwarf (Jordan et al. 2012; Kromer et al. 2013; Fink et al. 2014). However, several other explosion models have been proposed to explain the observational

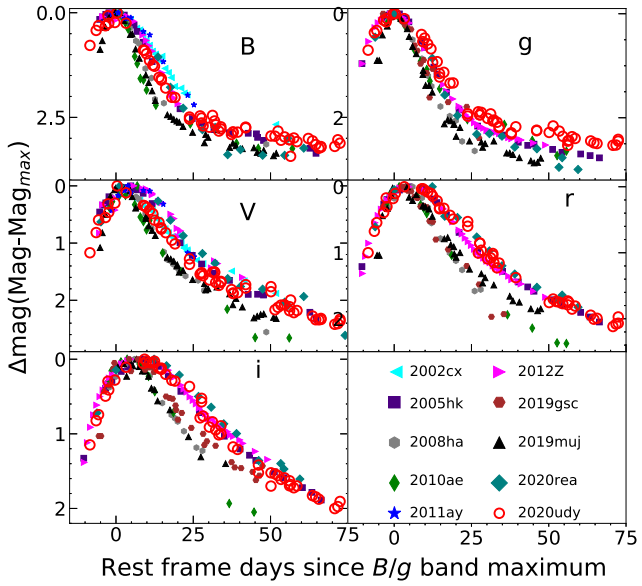

Figure 3. Light-curve comparison of SN 2020udy with other type Iax SNe. The date of maximum in the *B* band is used as a reference for comparison plots in *B* and *V* bands, while comparison plots in *gri* bands are with respect to the *g*-band maximum.

properties of bright type Iax SNe, such as pulsational delayed detonation (PDD, Baron et al. 2012; Dessart et al. 2014), deflagration to detonation transition (DDT, Seitenzahl et al. 2013; Sim et al. 2013), etc. The deflagration of a CO white dwarf cannot explain the observables of faint members of this class. Instead, they can be explained by the deflagration of a hybrid carbon–oxygen–neon white dwarf (Meng & Podsiadlowski 2014; Kromer et al. 2015).

SN 2020udy was spotted by Nordin & Perley (2020) using automated detection software AMPEL (Nordin et al. 2019) in association with the Zwicky Transient Facility (ZTF, Bellm et al. 2019; Fremling et al. 2020) on 2020 September 24 and was classified as type Iax SN (Nordin et al. 2020a, 2020b). The SN exploded in the spiral galaxy NGC 0812 at a redshift of 0.017222 (Falco et al. 1999). The SN was located at R.A. (J2000.0) $02^{h}06^{m}49^{s}.35$, decl.(J2000.0) $44°35'15''.29$, $52''.82$ N and $23''.13$ W from the center of the host galaxy.

Maguire et al. (2023) have presented an analysis of SN 2020udy. The very early detection of the SN allowed them to place strict limits on companion interaction. They ruled out the possibility of a main-sequence star with a mass of 2 or 6 $M_{\odot}$ being the companion; however, a helium star with a narrow range of viewing angle is suggested as a probable companion. They have shown that the light curve and spectra of SN 2020udy are in good agreement with the deflagration model of a CO white dwarf, specifically the N5-def model of Fink et al. (2014).

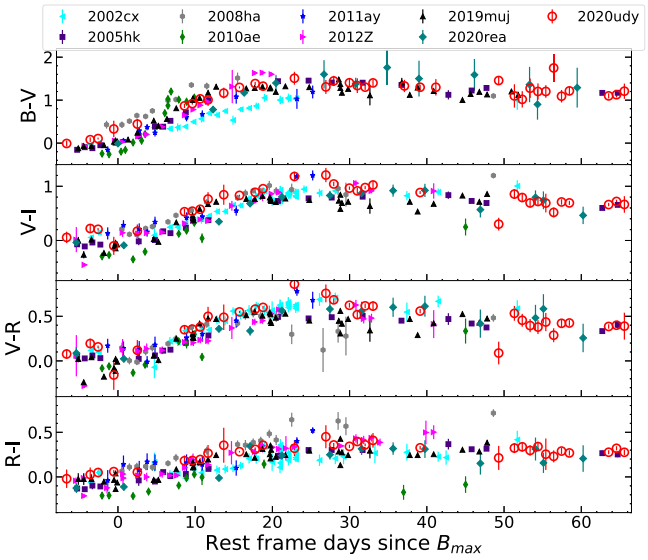

Figure 4. Color evolution of SN 2020udy with those of other type Iax SNe.

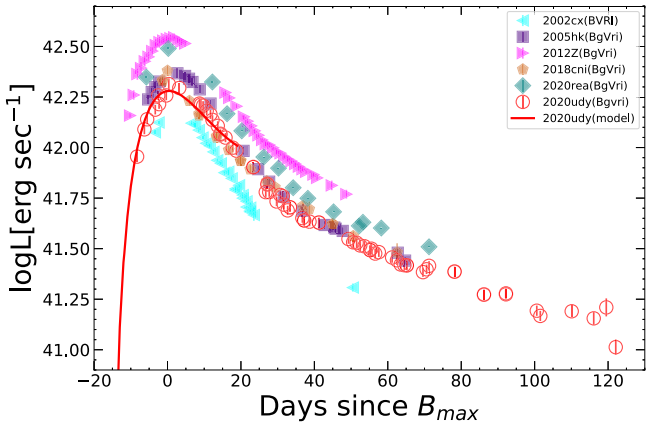

Figure 5. The pseudo-bolometric light curve of SN 2020udy and those of other type Iax SNe. The analytical model used to estimate the explosion parameters is shown by a solid line.

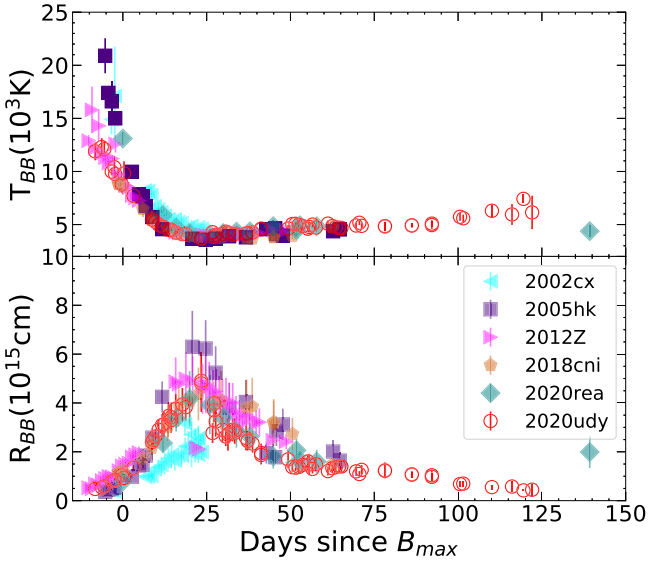

Figure 6. Evolution of blackbody temperature (T_{BB}, upper panel) and radius (R_{BB}, lower panel) of SN 2020udy compared to that of several other bright type Iax SNe.

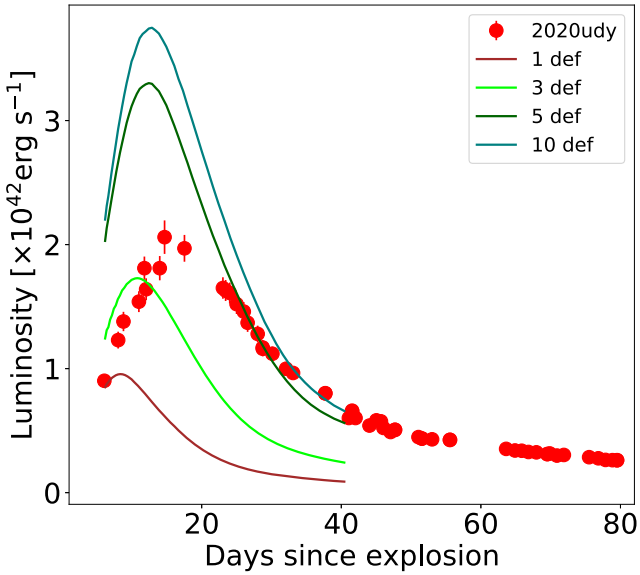

Figure 7. Comparison of the pseudo-bolometric light curve of SN 2020udy with the evolution of the optical bolometric luminosity of different deflagration models presented in Fink et al. (2014).

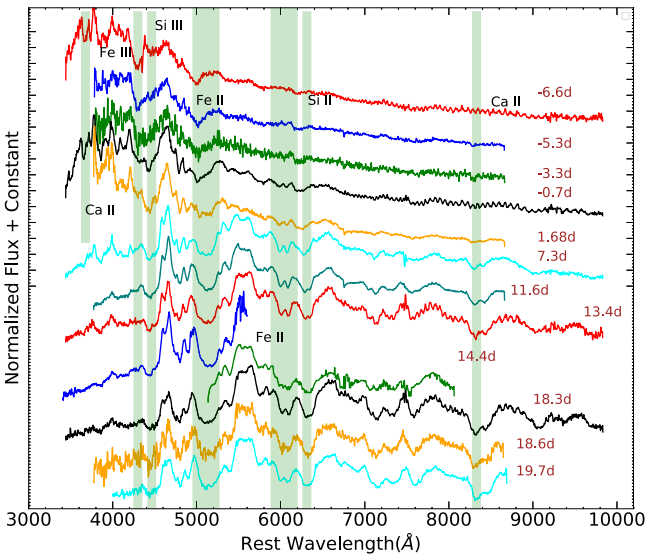

Figure 8. Spectral evolution of SN 2020udy from −6 to ∼20 days since the maximum.

(The data used to create this figure are available.)

This paper presents a detailed photometric and spectroscopic analysis of SN 2020udy. The light curve has been modeled using the analytical prescription proposed by Arnett (1982) and Valenti et al. (2008). To confirm the line identification and expansion velocity of the ejecta, the early spectral sequence is modeled with SYNAPPS. The one-dimensional radiative transfer code TARDIS has been used to perform abundance tomography modeling of the entire observed spectral sequence. Section 2 gives details about observations and methods used to reduce the data of SN 2020udy. In Section 3 we estimate the distance, the explosion time, and the line-of-sight extinction of the SN. Section 4 presents the photometric properties and the modeling of the pseudo-bolometric light curve of SN 2020udy. Spectroscopic features of SN 2020udy, the evolution of the photospheric velocity, and spectral modeling are presented in

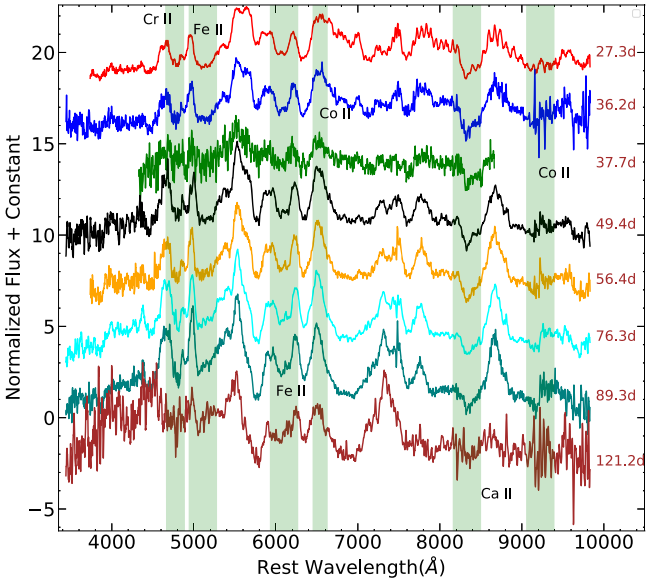

Figure 9. Spectral evolution of SN 2020udy spanning between 27 and 121 days since the maximum.

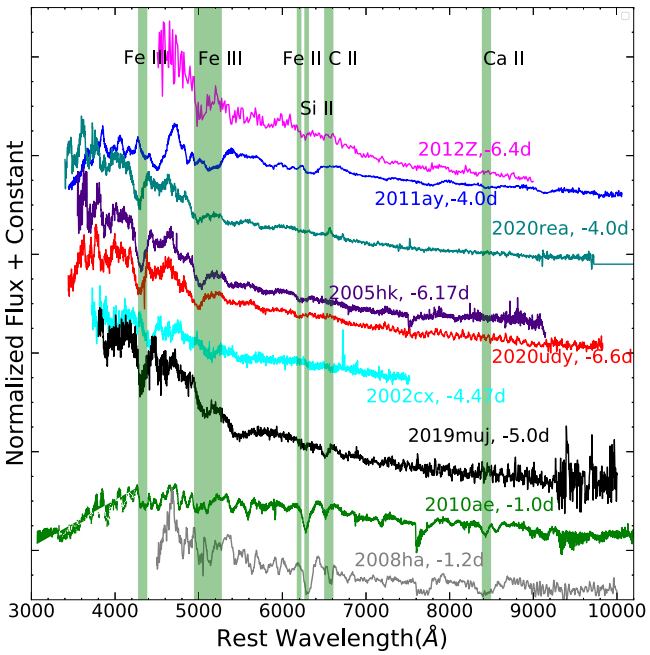

Figure 10. Pre-peak spectral features of SN 2020udy compared with those of other type Iax SNe at similar phases. The spectra are plotted in order of decreasing *B*-band peak brightness of the SNe.

Section 5. A brief discussion of the observational features of SN 2020udy and their comparison with a few explosion scenarios proposed for the type Iax class are given in Section 6. Section 7 summarizes our results.

2. Observations and Data Reduction

Optical photometric follow-up of SN 2020udy began ∼5 days after discovery and continued up to 130 days with the 1 m Las Cumbres Observatory (LCO) telescopes (Brown et al. 2013) under the Global Supernova Project and 80 cm Tsinghua-NAOC Telescope (TNT, Wang et al. 2008; Huang et al. 2012, National Astronomical Observatories of China).

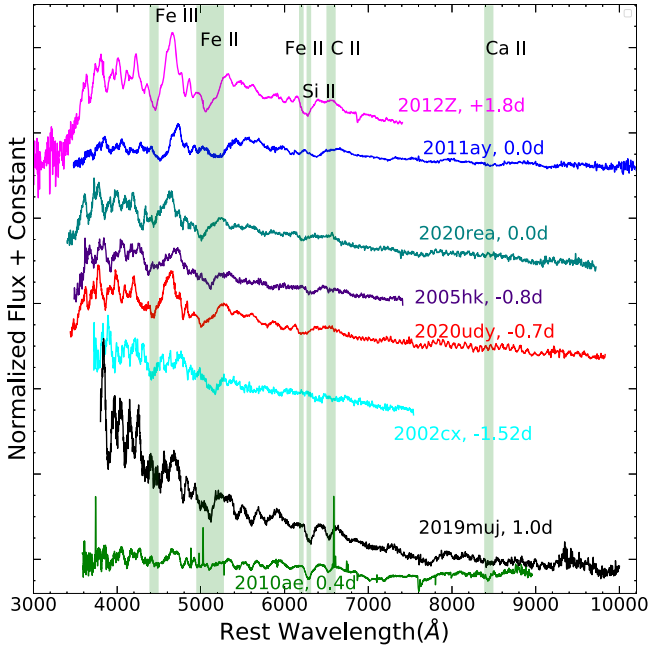

Figure 11. Comparison between the spectrum of SN 2020udy around the *B*-band peak brightness and those of other type Iax SNe observed at similar phases.

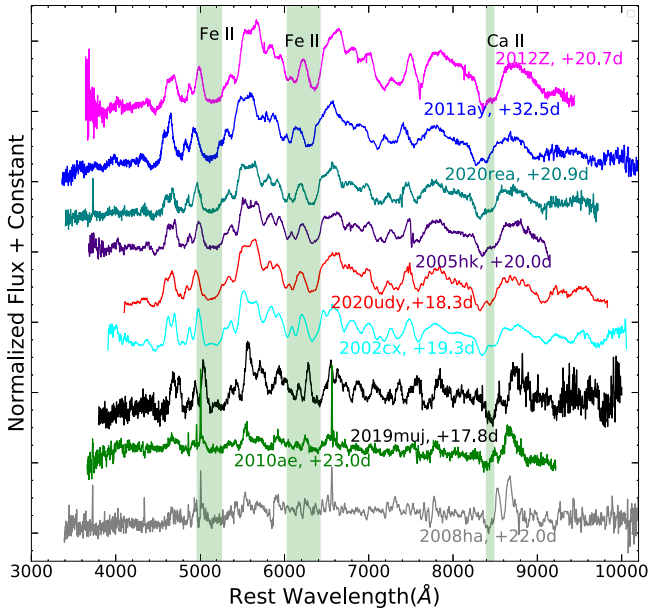

Figure 12. Comparison of post-peak spectral features of SN 2020udy with those of other type Iax SNe.

The observations were carried out in the *BgVri* photometric bands.

The LCO photometric data were reduced using the lcogtsnpipe routines (Valenti et al. 2016), which performs point-spread function photometry of the stars and the SN. The instrumental *BV* magnitudes were calibrated to the Vega system using the APASS catalog (Henden et al. 2016)[22] and the instrumental *gri* magnitudes were calibrated to the AB system

[22] https://www.aavso.org/aavso-photometric-all-sky-survey-data-release-1

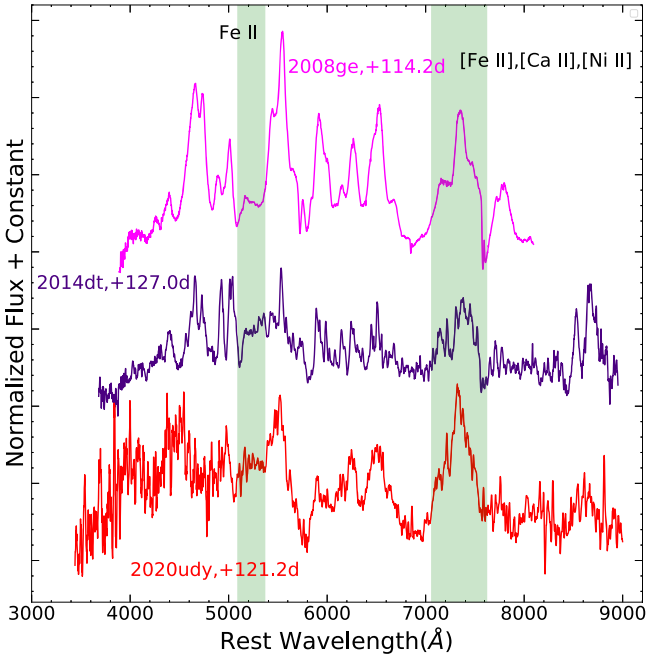

Figure 13. Comparison of nebular-phase spectral features of SN 2020udy with those of other type Iax SNe.

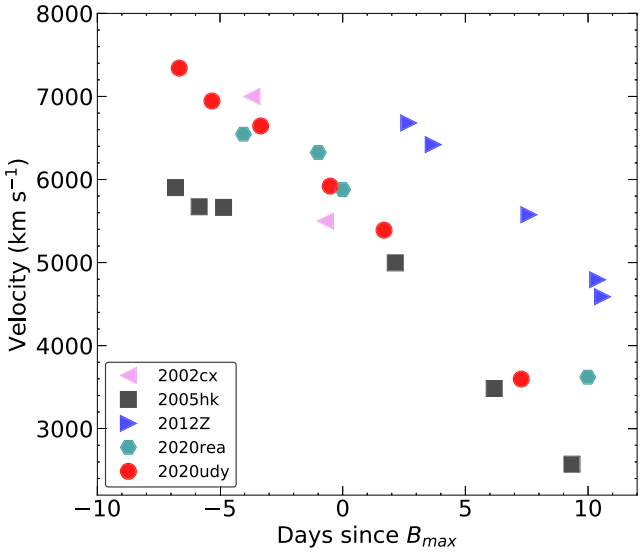

Figure 14. Evolution of the velocity of the Si II line in SN 2020udy with those of other type Iax SNe.

using the Sloan Digital Sky Survey (SDSS) catalog (Gunn et al. 2006).

The preprocessing of the photometric data obtained with the 80 cm TNT was carried out following standard procedures using a custom Fortran program. The photometry was then performed by the automatic pipeline ZrutyPhot (J. Mo et al., in preparation). The pipeline utilizes the Software for Calibrating Astrometry and Photometry (SCAMP, Bertin 2006) and the IRAF[23] Daophot package. The TNT instrumental *BV*

[23] IRAF stands for Image Reduction and Analysis Facility distributed by the National Optical Astronomy Observatory, operated by the Association of Universities for Research in Astronomy (AURA) under a cooperative agreement with the National Science Foundation.

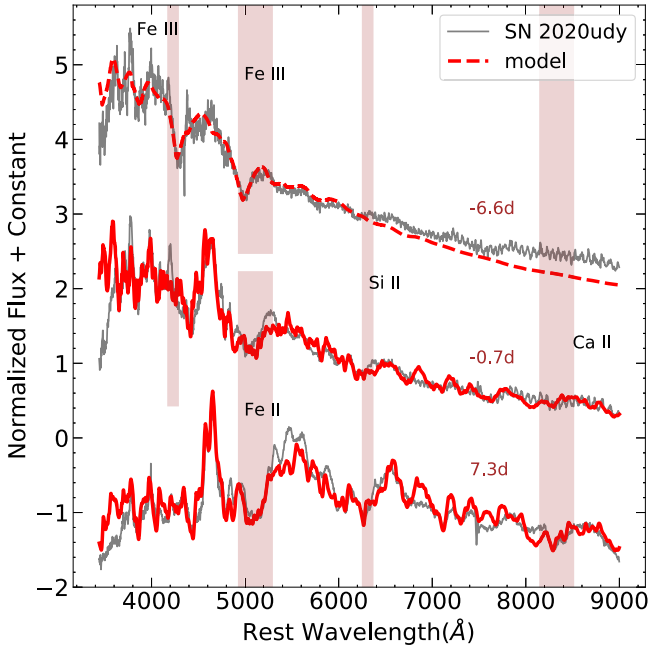

Figure 15. The spectra of SN 2020udy at −6.6, −0.7, and 7.3 days are shown (in gray) along with the respective SYNAPPS models (in red).

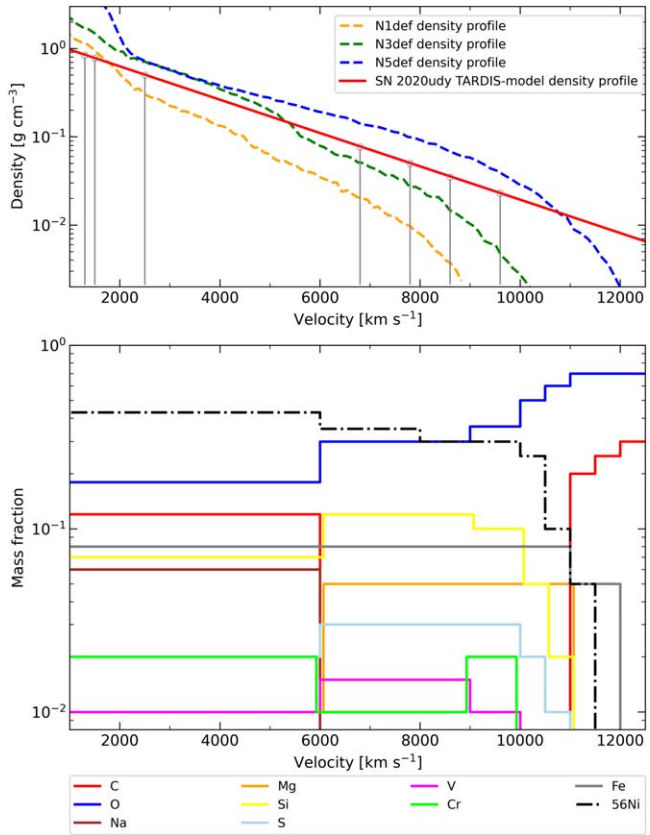

Figure 16. Top panel: the best-fit TARDIS density profile (red) compared to the pure deflagration at $t_0 = 100$ s. The gray lines indicate the location of the photosphere for each of the analyzed epochs. Bottom panel: the best-fit chemical abundance structure from the fitting process for the spectral sequence of SN 2020udy. The profile of the radioactive ^{56}Ni shows the mass fractions at $t_{exp} = 100$ s.

magnitudes of the SN were calibrated to the Vega system and the instrumental *gri* magnitudes were calibrated to the AB system using the PanSTARRS (Panoramic Survey Telescope

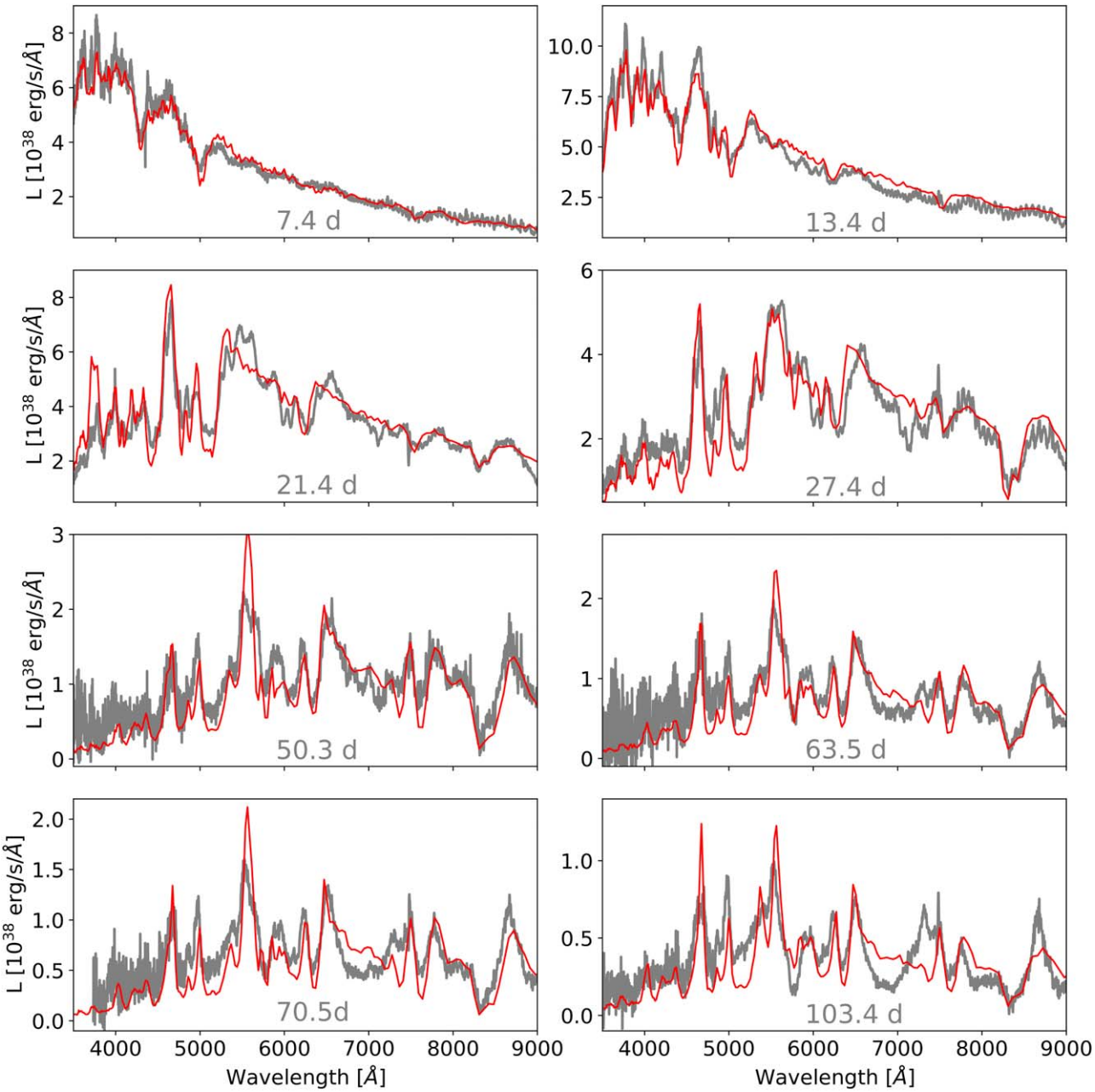

Figure 17. Spectral synthesis of the evolution of SN 2020udy. The model spectra (in red) are produced with `TARDIS` within the framework of the abundance tomography analysis.

and Rapid Response System[24]) catalog. The optical photometry of SN 2020udy is tabulated in Table 1. The errors mentioned in Table 1 are obtained by propagating the photometric and calibration errors in quadrature.

The spectroscopic observations of SN 2020udy, spanning up to ∼121 days after the maximum, were obtained with the LCO 2 m Faulkes Telescope North (FTN) in Hawaii, the Beijing Faint Object Spectrograph and Camera (BFOSC), mounted on the Xinglong 2.16 m telescope of NAOC (XLT; Fan et al. 2016), and the Dual Imaging Spectrograph (DIS) on the 3.5 m telescope (Astrophysical Research Consortium, ARC) at the Apache Point Observatory. The 1D wavelength and flux-calibrated LCO spectra were extracted using the `floydsspec` pipeline[25] (Valenti et al. 2014). The wavelength calibration of the BFOSC data and DIS data was done using Fe/Ar and He/Ar arc lamp spectra, respectively. The flux calibration was performed using spectra of standard stars that had similar airmass to that of the SN. All the spectra were scaled with the photometry to correct for slit loss. Finally, the spectra were corrected for the heliocentric redshift of the host galaxy. The log of spectroscopic observations is given in Table 2.

3. Distance, Extinction, and Explosion Epoch

3.1. Distance and Extinction

There are eight different distance estimates available for the host galaxy of SN 2020udy using the Tully–Fisher method (Karachentsev et al. 2006; Theureau et al. 2007; Tully et al. 2013, 2016; Sorce et al. 2014). Out of these, we have

[24] https://catalogs.mast.stsci.edu/panstarrs
[25] https://github.com/svalenti/FLOYDS_pipeline

used four recent measurements and scaled them to $H_0 = 73.00\ \mathrm{km\ s^{-1}\ Mpc^{-1}}$ (Spergel et al. 2007). The average of these four estimates, 56.20 ± 12.48 Mpc (consistent with Maguire et al. 2023), is used in this work.

The SN is located in the outskirts of the host galaxy, so significant reddening from the host galaxy is not expected. Also, in the spectral sequence of SN 2020udy, we do not find the Na I D feature associated with the host galaxy. Hence, for reddening correction, we have used only the extinction within the Milky Way, which is $E(B-V) = 0.067$ mag ($A_v = 0.210$ mag) (Schlafly & Finkbeiner 2011).

3.2. Explosion Epoch

The first ZTF *r*-band detection at JD 2459116.8 with the last nondetection in the *g* band 0.87 days ago, together with the comprehensive sampling of SN 2020udy in ZTF *gr* bandpasses during a few weeks before its explosion, allows a careful inspection of the time of its explosion. Assuming SN 2020udy exploded as an expanding fireball whose luminosity scales with its surface area, the flux (F) thus increases with the square of the time after the explosion (i.e., $F \propto (t - t_{\mathrm{exp}})^2$, Arnett 1982; Riess et al. 1999; Nugent et al. 2011). Hence, we use Equation (1) to fit the extinction-corrected flux in ZTF *g* and *r* bands, separately:

$$F_{\mathrm{band}} = A \times (t - t_{\mathrm{exp}})^n\ , \tag{1}$$

where A is a scale factor and the power-law index n has been fixed to 2 in the initial fitting, which gives $t^g_{\mathrm{exp}} =$ JD 2459111.9 ± 0.6 and $t^r_{\mathrm{exp}} =$ JD 2459113.3 ± 0.4. Such a $\approx$1.4 day discrepancy contradicts the last nondetection in the *g* band at JD 2459115.9 (see Figure 1).

Deviation from the $n = 2$ expanding fireball during the early-rising phase of type Iax SNe has been reported for multiple cases (Magee et al. 2016; Miller et al. 2020). In the next iteration of fitting, we thus kept n as a free parameter. This resulted in estimates of explosion epochs that were off by 0.5 days between both the bands with $n_g = 0.91 \pm 0.05$ and $n_r = 1.09 \pm 0.04$.

Further, we fit both the light curves iteratively by varying n simultaneously for both the bands in such a way that for the same value of n, which is a free parameter as before, they converge to the same explosion epoch.

We found that both the light curves converge to the same explosion epoch ($t_{\mathrm{exp}} =$ JD 2459116.2 ± 0.1) for $n = 1.03$. Maguire et al. (2023) quote a similar value for explosion epoch (JD 2459115.7 ± 0.1), but they estimated the power index $n \sim 1.3$ using a modified functional form. In this work, we use JD 2459116.2 ± 0.1 as the explosion date.

4. Light-curve Properties

4.1. Light Curve and Color Curve

Figure 2 presents the *BgVri*-band photometry of SN 2020udy. The light curves are well sampled around the SN peak brightness in all bandpasses. We use a cubic spline fit to estimate the time and magnitude at maximum light in the *BgVri* bands; the decline in magnitude from the light-curve peak to 15 days after (i.e., Δm_{15}) is also estimated for these bands (Table 3).

In Figure 3 we compare the light curves of SN 2020udy with several other well-sampled type Iax SNe: SNe 2002cx (Li et al. 2003), 2005hk (Sahu et al. 2008), 2008ha (Foley et al. 2009), 2010ae (Stritzinger et al. 2014), 2011ay (Stritzinger et al. 2015), 2012Z (Stritzinger et al. 2015), 2019gsc (Srivastav et al. 2020; Tomasella et al. 2020), 2019muj (Barna et al. 2021b), and 2020rea (Singh et al. 2022). The light curves are normalized to their peak magnitudes in the respective bands and plotted in the rest frame of the individual SN. In the *B* band, SN 2020udy declines more slowly than SNe 2002cx and 2011ay and its light-curve shape looks remarkably similar to those of SNe 2012Z and 2020rea. In the *g* band, SN 2020udy declines more slowly than all the comparison SNe. The evolution of the *V*-band light curve of SN 2020udy is faster than those of SNe 2002cx, 2005hk, 2011ay, 2012Z, and 2020rea but slower than those of the other SNe presented in our sample. With a slower decline in *r* and *i* bands, SN 2020udy appears to be very similar to SNe 2012Z and 2020rea (Figure 3).

The evolution of $B-V$, $V-I$, $V-R$, and $R-I$ colors of SN 2020udy and its comparison with that of other type Iax SNe has been depicted in Figure 4. All the colors are corrected for total reddening and brought to the rest frame of each SN. The color evolution of SN 2020udy seems to follow the same pattern as other type Iax SNe used for comparison.

4.2. Analysis of Bolometric Light Curve

The pseudo-bolometric *BgVri* light curve of SN 2020udy is constructed using `SuperBol` (Nicholl 2018), adopting the distance and extinction discussed in Section 3.1. In `SuperBol`, the dereddened magnitudes and associated errors of the SN are converted to fluxes and flux errors. These fluxes are used to construct the spectral energy distributions (SEDs) at all epochs, which are integrated using the trapezoidal rule in the limit of the input passbands to obtain the pseudo-bolometric luminosity. The flux errors and bandwidths are used to calculate the corresponding pseudo-bolometric luminosity error. The integration spans the wavelength range between 3960 and 8120 Å. To estimate the missing flux in the UV and near-IR (NIR) regions, `SuperBol` fits blackbody functions to the SED at each epoch and applies this correction to the pseudo-bolometric luminosities to construct the total bolometric luminosity. Figure 5 shows the pseudo-bolometric light curve of SN 2020udy along with a those of few other bright type Iax SNe. The pseudo-bolometric light curves of all the SNe presented in Figure 5 are constructed similarly. We have added another bright type Iax SN, 2018cni (Singh et al. 2023), for comparison in Figure 5. Around maximum, SN 2020udy looks slightly fainter than SNe 2005hk and 2018cni but after $\sim$10 days their pseudo-bolometric luminosities are comparable. This shows that SN 2020udy is a bright type Iax SN with peak (*BgVri*) luminosity of $(2.06 \pm 0.14) \times 10^{42}\ \mathrm{erg\ s^{-1}}$.

To estimate the explosion parameters, such as the mass of ^{56}Ni and ejecta mass (M_{ej}), we employed an analytical model proposed by Arnett (1982) and Valenti et al. (2008). This model assumes spherically symmetric and optically thick ejecta, a small initial radius, constant optical opacity, and the presence of ^{56}Ni in the ejected matter. We fitted the pseudo-bolometric light curve with the analytical model using the scipy.optimize.curve_fit algorithm, setting κ_{opt} to $0.1\ \mathrm{cm^2\ g^{-1}}$ and the photospheric velocity to $8000\ \mathrm{km\ s^{-1}}$ at maximum. From the fitting, we obtained the following values of the parameters: ^{56}Ni mass $= 0.08 \pm 0.01\ M_\odot$ and ejecta mass $(M_{\mathrm{ej}}) = 1.39 \pm 0.09\ M_\odot$, with the errors obtained from the covariance matrix.

The bolometric rise time obtained through this fit is ∼15 days. This is consistent with the rise time estimated independently by fitting the early light curves of SN 2020udy (see Section 3.2).

To obtain the total bolometric luminosity from the pseudo-bolometric luminosity, the contribution from the missing bands needs to be added. For type Iax SNe, the exact contribution of UV and NIR fluxes to the total bolometric luminosity is not known, because both UV and NIR coverage are available for only a handful of objects in the literature (Phillips et al. 2007; Yamanaka et al. 2015; Tomasella et al. 2016; Srivastav et al. 2020, 2022; Dutta et al. 2022). Based on the available estimates, if the contribution from UV and NIR bands to the total luminosity at maximum is taken as ∼35%, the mass of ^{56}Ni increases to 0.11 $M_{\odot}$.

Figure 6 compares the evolution of the blackbody temperature and radius of SN 2020udy with that estimated for several other well-studied type Iax SNe. The blackbody temperature evolves in a similar fashion for all the type Iax SNe presented in Figure 6, whereas the blackbody radius is proportional to the luminosity of the SN.

In Figure 7, we compare the pseudo-bolometric luminosity of SN 2020udy with deflagration models presented in Fink et al. (2014). The model light curves N1-def, N3-def, N5-def, and N10-def are adopted from the HESMA database. The numerical value indicates the number of ignition spots of the model, which approximately scales with the strength of the deflagration. During the photospheric phase, the pseudo-bolometric luminosity of SN 2020udy lies between the N3-def and N5-def models. Around 30 days post-explosion, SN 2020udy shows a slower decrease in the bolometric luminosity than all the models presented in Figure 7, which may indicate a higher ejecta mass of SN 2020udy compared to the model predictions.

5. Spectral Evolution

5.1. Spectral Features of SN 2020udy and Their Comparison with Other Type Iax SNe

Figures 8 and 9 present the spectroscopic evolution of SN 2020udy spanning from −6.6 to +121.2 days relative to its *B*-band maximum light. During the pre-maximum phase, the spectra of SN 2020udy show a blue continuum with features due to Ca II H&K, Fe III, Si III, Fe II, and Si II. Prominent P-Cygni profiles with a broad absorption component can also be identified. Similar to other bright type Iax SNe, SN 2020udy also exhibits a rather shallow Si II absorption line at 6355 Å. We do not detect the C II feature at 6580 Å. Figure 10 presents a comparison of the earliest spectrum of SN 2020udy at −6.6 days with several other type Iax SNe observed at similar phases. Fe III features near 4400 and 5000 Å are present in all the SNe. Additionally, we remark that the strength of both Si II and C II features diminishes with the increasing luminosity of type Iax SNe. For example, fainter events like SNe 2008 ha and 2010ae display significantly stronger Si II and obvious C II absorption lines compared to bright events such as SNe 2012Z, 2020rea, 2020udy, etc. Similarly, in faint type Iax SNe, the Ca II NIR feature also emerges earlier than in bright ones.

Comparison of spectral features near maximum (Figure 11) indicates a similarity between SN 2020udy and other bright type Iax SNe. Near maximum, the strength of the Si II 6355 Å line increases. Features due to Fe III near 4400 Å, Fe II near 5000 Å, Si II, and the Ca II NIR triplet are prominently seen in all the SNe. In the early post-maximum phase (∼7 days), the blue part of the spectrum gets suppressed because of cooling of the ejecta and line blanketing (Figure 8). With time, the Si II line is replaced by the progressively emerging Fe/Co lines (Figure 9). The features between 5500 and 7000 Å are mostly dominated by Fe II lines.

Post-maximum (after ∼20 days since maximum) spectral evolution of SN 2002udy is shown in Figure 9. The Cr II feature near 4800 Å and Co II feature near 6500 Å are clearly visible. The Ca II NIR triplet becomes progressively stronger. Figure 12 compares the spectrum of SN 2020udy obtained at day +18.3 with the spectra of other type Iax SNe at similar phases. The spectra of all SNe in the sample are dominated by iron group elements (IGEs). SN 2020udy exhibits remarkable similarities to bright type Iax SNe such as SNe 2005hk, 2011ay, and 2020rea. An absorption feature at ∼9000 Å, due to Co II, is also seen in SN 2020udy. As the inner ejecta of the SN becomes optically thin during the late phase, emission lines increase in strength.

In the late phase, spectral features become narrow (Figure 9). The region around 7300 Å is composed of forbidden lines of Fe/Ni and Ca (Foley et al. 2016). The presence of both forbidden and permitted lines in the late-phase spectra of SN 2020udy indicates that the spectrum is not fully nebular. Type Iax SNe possess a long-lived photosphere with the presence of permitted lines even at late times (Jha et al. 2006b; Sahu et al. 2008; Foley et al. 2010a, 2016). Figure 13 shows a nebular-phase spectral comparison between SNe 2020udy, 2008ge (Foley et al. 2010b), and 2014dt (Singh et al. 2018) at comparable epochs. The nebular-phase spectra of SN 2020udy and SN 2008ge (Foley et al. 2010b) show broad emission features, while SN 2014dt has narrow spectral features. Maguire et al. (2023) have also reported broad emission features in the spectrum of SN 2020udy at ∼119 and 137 days and suggested that they might be coming from the SN ejecta. In the case of SN 2012Z, similar broad emission features were reported at a very late phase (∼190 days, Stritzinger et al. 2015). Foley et al. (2016) suggested that relatively bright type Iax SNe with higher ejecta velocities exhibit broad forbidden lines; SN 2020udy is consistent with these findings.

5.2. Evolution of Photospheric Velocity

Figure 14 displays the photospheric expansion velocity of SN 2020udy traced by the evolution of the Si II line at 6355 Å and that measured for several other type Iax SNe. We estimate the expansion velocity by fitting a Gaussian profile to the absorption minimum of the Si II line. The expansion velocity of SN 2020udy around maximum light is ∼6000 km s^{-1}. Between −6.6 and +7.27 days, the photospheric velocity of SN 2020udy is similar to that of SN 2020rea, higher than that of SN 2005hk, and lower than that of SN 2012Z. The photospheric velocity estimated from the absorption minimum of the Si II line at 6355 Å becomes unreliable after about two weeks relative to the *B*-band peak brightness due to the increasing blending with the emerging iron lines. Type Iax SNe having higher luminosity are known to have high photospheric velocity (McClelland et al. 2010; Foley et al. 2013) except for a few outliers. We found that SN 2020udy is consistent with such a correlation between luminosity and velocity.

5.3. Spectral Modeling

5.3.1. Spectral Modeling with SYNAPPS

Photospheric spectra of SN 2020udy at three epochs, i.e., −6.6, −0.7, and 7.3 days relative to the *B*-band peak brightness, are modeled using the spectrum synthesis code SYNAPPS (Thomas et al. 2011) and are shown in Figure 15. The photospheric velocity in the best-fit model falls from 11,250 km s^{-1} at −6.6 days to 6570 km s^{-1} at 7.3 days. The outer ejecta velocity used in the modeling is 30,000 km s^{-1}. The photospheric temperature evolves from 12,200 K at −6.6 days to 8500 K at 7.3 days. The chemical species used in the modeling are Fe, Si, Ca, Mg, and S. Specifically, in the pre-maximum spectral fitting, we used S II, Si II, Si III, Mg II, Ca II, Fe II, and Fe III ions. The prominent Fe II and Fe III features in the pre-maximum spectrum are reproduced very well in the models. In the model spectra at maximum and post-maximum, most of the spectral features such as Fe, Si, Ca, etc., match well with our observed spectra.

5.3.2. Spectral Modeling with TARDIS

We perform spectral modeling for SN 2020udy using the one-dimensional radiative transfer code TARDIS, following the principles of abundance tomography. The setting of TARDIS and the fitting strategy is almost the same as in our previous study, where SNe 2018cni and 2020kyg were the subjects of analysis (Singh et al. 2023). The method was previously applied for abundance tomography of normal SNe Ia using artificial intelligence-assisted inversion (Chen et al. 2020, 2024) and the fit-by-eye method (Barna et al. 2021a) as well, providing similar abundance profiles and the same goodness of fit.

The present spectral synthesis covers a longer time, ∼90 days after the maximum. Camacho-Neves et al. (2023) showed that radiative transfer codes that assume a blackbody-emitting photosphere can reproduce most of the spectral features and their evolution over years after the explosion because type Iax SNe never show a fully nebular spectrum. At the same time, spectral synthesis is less sensitive to the exact mass fractions of chemical elements at $t_{\rm exp} > 30$ days than at the earlier epochs. The information is retrievable from late-time spectral fitting limits to luminosity (L) and photospheric velocity ($v_{\rm phot}$), and identification of the presence of chemical elements.

The abundance tomography presented in this study is split into two parts: before $t_{\rm exp} = 30$ days from the date of explosion (hereafter referred to as early epochs), we follow the standard technique for synthesizing a spectral time series (Singh et al. 2023), while for the later epochs, a simplified method is adopted similar to that of Camacho-Neves et al. (2023). For both phases, the same time of the explosion ($t_{\rm exp}$ = JD 2459116.3), which is within the uncertainty range of the time derived from early light-curve synthesis (see Section 3.2), and density profile are used for the fit of any epochs. The latter is chosen as a simple exponential function and constrained from the fitting as

$$\rho(v, t_{\rm exp}) = \rho_0 \times \left(\frac{t_{\rm exp}}{t_0}\right)^{-3} \times \exp\left(-\frac{v}{v_0}\right), \quad (2)$$

where $\rho_0 = 1.4$ g cm^{-3} is the core density shortly after the time of the explosion ($t_{\rm exp}$) when the homologous expansion starts (here chosen as $t_0 = 100$ s), while $v_0 = 2300$ km s^{-1} is the exponential steepness of the density structure decreasing outwards. The chemical composition of ten elements (see Figure 16) is fit in radial shells with a velocity width of 500 km s^{-1}. Our initial assumption for each element's abundance was the constant fit of the abundance structure of the N5-def deflagration model (Fink et al. 2014). During the fitting process, we aimed for simplicity and modified the actual abundance structure of a shell only when the quality of the match between the synthetic and observed spectra is clearly improved with the change. At later epochs ($t_{\rm exp} > 30$ days), the minor changes in abundance have little or no impact on the outcome of the radiative transfer, thus we fixed the initially assumed constant values with minor modifications regarding the presence of lines of certain elements (see below). Note that despite several simplifications, the number of fitting parameters is far too high to fully cover the parameter space, thus our "best-fit" model can be considered as a feasible solution at its best.

The synthetic spectra are displayed in Figure 17. The dominant spectral features of SN 2020udy are reproduced by our final model at every epoch. The absorption profiles of IMEs such as Si, S, Ca, etc., are nicely fitted at all phases. As an observable weakness of the fits, the P-Cygni features of IGEs after 20 days are overestimated in general (see between 4000 and 5500 Å in Figure 17). However, the fix of this issue involves either reduced Fe and ^{56}Ni abundances or lower v_0 to decrease the outer densities; but both options would reduce the goodness of the fits at other epochs.

The best-fit density profile (upper panel of Figure 16) shows the same steepness ($v_0 = 2300$ km s^{-1}) as that of other type Iax SNe, which were the subject of similar abundance tomography analysis (Barna et al. 2018, 2021b). The inferred $\rho(v)$ function scales the densities between those of the N3-def and N5-def models during the early epochs, which is consistent with Figure 7. The constrained abundance structure shows a strong stratification of both the IGE and IME mass fractions that reproduce the fast evolution of spectral lines. As a further contradiction to the pure deflagration models, C is not allowed below 11,000 km s^{-1} in our model to prevent the appearance of extremely strong C II λ4618 and λ6578 lines. The possible detection of such stratification in the outermost region of type Iax SNe is not unprecedented in the literature (see, e.g., Seitenzahl et al. 2013; Barna et al. 2018), but studies with other methodologies of spectral synthesis argued against chemical layering (Magee et al. 2022). Note that due to the high level of degeneracy of our fitting process, the results regarding the stratification are inconclusive. Optical spectroscopy at even earlier phases ($t_{\rm exp} < 4$ days) and/or UV spectral observations are required to resolve this issue.

The fits of the late-time epochs (below ∼6000 km s^{-1}) support the existence of a uniform chemical structure in the inner ejecta (Fink et al. 2014). Similar to Camacho-Neves et al. (2023), we set a high Na mass fraction to produce the P-Cygni feature at ∼5800 Å. As a further modification, we increase the abundance of V and Cr to create the features observed around ∼4000 and ∼5800 Å respectively. While the overabundance of Na is well justified by the unambiguous identification, similar to that of the extremely late-time spectral synthesis of SN 2014dt, the presence of Cr and V with mass fractions of 1%–2% is not conclusive.

6. Discussion

The relatively complete photometric coverage of pre-maximum evolution of SN 2020udy allows us to constrain its rise time to ∼15 days in the B band, which is similar to that of SN 2005hk (Phillips et al. 2007). Our analysis of the pseudo-bolometric light curve of SN 2020udy estimates the ^{56}Ni mass as $0.08 \pm 0.01\ M_{\odot}$ and the ejecta mass as $1.39 \pm 0.09\ M_{\odot}$. Comparison of the pseudo-bolometric light curves of SN 2020udy with different deflagration models shows that SN 2020udy lies between N3-def and N5-def models during the photospheric phase. The spectroscopic features and the evolution of photospheric velocity of SN 2020udy are similar to those of other bright type Iax SNe. The late nebular-phase spectral features of SN 2020udy are broad and similar to those of SN 2012Z. To ascertain the most probable explosion scenario/progenitor system, we compare the observational properties of SN 2020udy with different proposed models for type Iax SNe.

The PDD scenario starts with a slow deflagration that expands the white dwarf. Subsequently, the infalling C–O layer triggers detonation (Ivanova et al. 1974; Khokhlov 1991a, 1991b; Khokhlov et al. 1993; Hoeflich et al. 1995; Hoeflich & Khokhlov 1996; Bravo & García-Senz 2006; Baron et al. 2012; Dessart et al. 2014). The mass of ^{56}Ni estimated in SN 2020udy is less than the mass of ^{56}Ni produced in the PDD scenario (0.12–0.66 $M_{\odot}$, Hoeflich et al. 1995). The observed $(B-V)$ color (0.33 mag) of SN 2020udy at maximum is slightly bluer than the $(B-V)$ color (0.44 mag, Hoeflich et al. 1995) expected in the PDD54 model.

In DDT models (Khokhlov 1991a, 1991c; Khokhlov et al. 1993; Hoeflich et al. 1995; Hoeflich & Khokhlov 1996; Höflich et al. 2002; Seitenzahl et al. 2013; Sim et al. 2013), a deflagration flame is ignited by nuclear burning followed by expansion of the star. A considerable amount of the fuel burns into IMEs at lower ignition densities. Subsequently, a detonation commences that consumes most of the fuel. The mass of synthesized ^{56}Ni in the case of SN 2020udy ($0.08 \pm 0.01\ M_{\odot}$) is significantly less than the expected mass of synthesized ^{56}Ni produced in the DDT explosion (0.32–1.1 $M_{\odot}$, Sim et al. 2013). Although the $(B-V)$ color of SN 2020udy (0.33 mag) at maximum falls in the range of the DDT models (0.15–0.56 mag), other parameters such as the B-band absolute magnitude of SN 2020udy ($M_{B,\max} = -17.41 \pm 0.34$ mag) are not consistent with the DDT model prediction (∼−19.93 to −18.16 mag).

The three-dimensional pure deflagration of a white dwarf yields a range of synthesized ^{56}Ni mass of 0.03–0.38 $M_{\odot}$ (Fink et al. 2014). The rise time and peak absolute magnitudes provided by these models fall in the ranges 7.6–14.4 days and −16.84 to −18.96 mag, respectively. Most of the observed parameters of SN 2020udy fit well within the range of parameters predicted by such a 3D pure deflagration process. Type Iax SNe are considered to be a heterogeneous class; the progenitor and explosion scenario at the two extreme ends of the luminosity distribution are shown to be different. However, bright members of this class (excluding outliers) behave in a similar manner and most of the observed properties of other bright type Iax SNe, such as SNe 2020rea (Singh et al. 2022), 2020sck (Dutta et al. 2022), etc., are consistent with the pure deflagration of a white dwarf in 3D (Fink et al. 2014). Based on the comparison of bolometric light curves and the density structure constrained from the abundance tomography analysis, SN 2020udy resembles a transition between the N3-def and N5-def pure deflagration models (Fink et al. 2014).

7. Summary

The extensive photometric and spectroscopic follow-up of SN 2020udy reveals the following features.

1. SN 2020udy is a bright member of the type Iax class with $M_{B,\max} = -17.41 \pm 0.34$ mag.
2. The analytical modeling of the pseudo-bolometric light curve yields $0.08 \pm 0.01\ M_{\odot}$ of synthesized ^{56}Ni with a well constrained rise time of ∼15 days.
3. Spectroscopic features of SN 2020udy show similarity with those of the other bright members of the type Iax class.
4. Abundance tomography modeling of SN 2020udy shows a photospheric velocity of $\sim 8000\ \mathrm{km\ s^{-1}}$ at maximum. This fits into the general trend of the Iax class, as brighter objects expand with higher velocity.
5. Comparison of proposed explosion models with the observational parameters shows that SN 2020udy is consistent with explosion models of pure deflagration of a white dwarf.
6. While the earliest spectra, which sample the outermost layers of the ejecta, show some indications of chemical stratification, the post-maximum evolution of SN 2020udy is consistent with the predictions of the pure deflagration scenario.
7. Thus, SN 2020udy is an addition to the bright type Iax SNe population. The observed similarities of SN 2020udy with other bright type Iax SNe indicate homogeneity within bright members of this class.

Acknowledgments

We thank the anonymous referee for providing useful comments and suggestions toward improvement of the manuscript. We acknowledge Wiezmann Interactive Supernova data REPository (WISeREP[26]; Yaron & Gal-Yam 2012). This research has made use of the CfA Supernova Archive, which is funded in part by the National Science Foundation through grant AST 0907903. This research has made use of the NASA/IPAC Extragalactic Database (NED) which is operated by the Jet Propulsion Laboratory, California Institute of Technology, under contract with the National Aeronautics and Space Administration. R.D. acknowledges funds by ANID grant FONDECYT Postdoctorado No 3220449. The work of X.W. is supported by the National Natural Science Foundation of China (NSFC grants 12288102, 12033003, and 11633002), the Science Program (BS202002) and the Innovation Project (23CB061) of Beijing Academy of Science and Technology, and the Tencent Xplorer Prize. This work makes use of data obtained with the LCO Network. This research made use of `TARDIS`, a community-developed software package for spectral synthesis in supernovae (Kerzendorf & Sim 2014; Kerzendorf et al. 2018, 2019). The development of `TARDIS` received support from the Google Summer of Code initiative and from ESA's Summer of Code in Space program. `TARDIS` makes extensive use of Astropy and PyNE. This work made

[26] http://wiserep.weizmann.ac.il

use of the Heidelberg Supernova Model Archive (HESMA).[27] D.A.H., G.H., and C.M. were supported by NSF grants AST-1313484 and AST-1911225. We acknowledge the usage of the HyperLeda database.[28] The SDSS is managed by the Astrophysical Research Consortium for the Participating Institutions. The Participating Institutions are the American Museum of Natural History, Astrophysical Institute Potsdam, University of Basel, University of Cambridge, Case Western Reserve University, University of Chicago, Drexel University, Fermilab, the Institute for Advanced Study, the Japan Participation Group, Johns Hopkins University, the Joint Institute for Nuclear Astrophysics, the Kavli Institute for Particle Astrophysics and Cosmology, the Korean Scientist Group, the Chinese Academy of Sciences (LAMOST), Los Alamos National Laboratory, the Max-Planck-Institute for Astronomy (MPIA), the Max-Planck-Institute for Astrophysics (MPA), New Mexico State University, Ohio State University, University of Pittsburgh, University of Portsmouth, Princeton University, the United States Naval Observatory, and the University of Washington.

ORCID iDs

Mridweeka Singh https://orcid.org/0000-0001-6706-2749
Devendra K. Sahu https://orcid.org/0000-0002-6688-0800
Barnabás Barna https://orcid.org/0000-0003-4769-4794
Anjasha Gangopadhyay https://orcid.org/0000-0002-3884-5637
Raya Dastidar https://orcid.org/0000-0001-6191-7160
Rishabh Singh Teja https://orcid.org/0000-0002-0525-0872
Kuntal Misra https://orcid.org/0000-0003-1637-267X
D. Andrew Howell https://orcid.org/0000-0003-4253-656X
Xiaofeng Wang https://orcid.org/0000-0002-7334-2357
Shengyu Yan https://orcid.org/0009-0004-4256-1209
Daichi Hiramatsu https://orcid.org/0000-0002-1125-9187
Craig Pellegrino https://orcid.org/0000-0002-7472-1279
G. C. Anupama https://orcid.org/0000-0003-3533-7183
Arti Joshi https://orcid.org/0000-0001-9275-0287
K. Azalee Bostroem https://orcid.org/0000-0002-4924-444X
Jamison Burke https://orcid.org/0000-0003-0035-6659
Curtis McCully https://orcid.org/0000-0001-5807-7893
Xin Li https://orcid.org/0000-0001-5879-8762
Shubham Srivastav https://orcid.org/0000-0003-4524-6883
Hyobin Im https://orcid.org/0000-0002-5742-8476
Anirban Dutta https://orcid.org/0000-0002-7708-3831

References

Arnett, W. D. 1982, ApJ, 253, 785
Barna, B., Pereira, T., Taubenberger, S., et al. 2021a, MNRAS, 506, 415
Barna, B., Szalai, T., Jha, S. W., et al. 2021b, MNRAS, 501, 1078
Barna, B., Szalai, T., Kerzendorf, W. E., et al. 2018, MNRAS, 480, 3609
Baron, E., Höflich, P., Krisciunas, K., et al. 2012, ApJ, 753, 105
Bellm, E. C., Kulkarni, S. R., Barlow, T., et al. 2019, PASP, 131, 068003
Bertin, E. 2006, in ASP Conf. Ser. 351, Astronomical Data Analysis Software and Systems XV, ed. C. Gabriel et al. (San Francisco, CA: ASP), 112
Bravo, E., & García-Senz, D. 2006, ApJL, 642, L157
Brown, T. M., Baliber, N., Bianco, F. B., et al. 2013, PASP, 125, 1031
Camacho-Neves, Y., Jha, S. W., Barna, B., et al. 2023, ApJ, 951, 67
Chen, X., Hu, L., & Wang, L. 2020, ApJS, 250, 12
Chen, X., Wang, L., Hu, L., & Brown, P. J. 2024, ApJ, 962, 125
Dessart, L., Blondin, S., Hillier, D. J., & Khokhlov, A. 2014, MNRAS, 441, 532
Dutta, A., Sahu, D. K., Anupama, G. C., et al. 2022, ApJ, 925, 217
Falco, E. E., Kurtz, M. J., Geller, M. J., et al. 1999, PASP, 111, 438
Fan, Z., Wang, H., Jiang, X., et al. 2016, PASP, 128, 115005
Fink, M., Kromer, M., Seitenzahl, I. R., et al. 2014, MNRAS, 438, 1762
Foley, R. J., Brown, P. J., Rest, A., et al. 2010a, ApJL, 708, L61
Foley, R. J., Challis, P. J., Chornock, R., et al. 2013, ApJ, 767, 57
Foley, R. J., Chornock, R., Filippenko, A. V., et al. 2009, AJ, 138, 376
Foley, R. J., Jha, S. W., Pan, Y.-C., et al. 2016, MNRAS, 461, 433
Foley, R. J., Rest, A., Stritzinger, M., et al. 2010b, AJ, 140, 1321
Foley, R. J., Van Dyk, S. D., Jha, S. W., et al. 2015, ApJL, 798, L37
Fremling, C., Miller, A. A., Sharma, Y., et al. 2020, ApJ, 895, 32
Greiner, J., Maitra, C., Haberl, F., et al. 2023, Natur, 615, 605
Gunn, J. E., Siegmund, W. A., Mannery, E. J., et al. 2006, AJ, 131, 2332
Henden, A. A., Templeton, M., Terrell, D., et al. 2016, yCat, II/336
Hoeflich, P., & Khokhlov, A. 1996, ApJ, 457, 500
Hoeflich, P., Khokhlov, A. M., & Wheeler, J. C. 1995, ApJ, 444, 831
Höflich, P., Gerardy, C. L., Fesen, R. A., & Sakai, S. 2002, ApJ, 568, 791
Huang, F., Li, J.-Z., Wang, X.-F., et al. 2012, RAA, 12, 1585
Ivanova, L. N., Imshennik, V. S., & Chechetkin, V. M. 1974, Ap&SS, 31, 497
Jacobson-Galán, W. V., Foley, R. J., Schwab, J., et al. 2019, MNRAS, 487, 2538
Jha, S., Branch, D., Chornock, R., et al. 2006a, AJ, 132, 189
Jha, S., Kirshner, R. P., Challis, P., et al. 2006b, AJ, 131, 527
Jha, S. W. 2017, in Handbook of Supernovae, ed. A. W. Alsabti & P. Murdin (Berlin: Springer), 375
Jordan, G. C., IV, Perets, H. B., Fisher, R. T., & van Rossum, D. R. 2012, ApJL, 761, L23
Karachentsev, I. D., Kudrya, Y. N., Karachentseva, V. E., & Mitronova, S. N. 2006, Ap, 49, 450
Karambelkar, V. R., Kasliwal, M. M., Maguire, K., et al. 2021, ApJL, 921, L6
Kerzendorf, W., Nöbauer, U., Sim, S., et al. 2018, tardis-sn/tardis: TARDIS v2.0.2 release, v2.0.2, Zenodo, doi:10.5281/zenodo.1292315
Kerzendorf, W., Nöbauer, U., Sim, S., et al. 2019, tardis-sn/tardis: TARDIS v3.0 alpha2, v3.0-alpha.2, Zenodo, doi:10.5281/zenodo.2590539
Kerzendorf, W. E., & Sim, S. A. 2014, MNRAS, 440, 387
Khokhlov, A., Mueller, E., & Hoeflich, P. 1993, A&A, 270, 223
Khokhlov, A. M. 1991a, A&A, 245, L25
Khokhlov, A. M. 1991b, A&A, 246, 383
Khokhlov, A. M. 1991c, A&A, 245, 114
Kromer, M., Fink, M., Stanishev, V., et al. 2013, MNRAS, 429, 2287
Kromer, M., Ohlmann, S. T., Pakmor, R., et al. 2015, MNRAS, 450, 3045
Li, L., Wang, X., Zhang, J., et al. 2018, MNRAS, 478, 4575
Li, W., Filippenko, A. V., Chornock, R., et al. 2003, PASP, 115, 453
Magee, M. R., Gillanders, J. H., Maguire, K., Sim, S. A., & Callan, F. P. 2022, MNRAS, 509, 3580
Magee, M. R., Kotak, R., Sim, S. A., et al. 2016, A&A, 589, A89
Magee, M. R., Kotak, R., Sim, S. A., et al. 2017, A&A, 601, A62
Magee, M. R., Sim, S. A., Kotak, R., Maguire, K., & Boyle, A. 2019, A&A, 622, A102
Maguire, K., Magee, M. R., Leloudas, G., et al. 2023, MNRAS, 525, 1210
McClelland, C. M., Garnavich, P. M., Galbany, L., et al. 2010, ApJ, 720, 704
McCully, C., Jha, S. W., Foley, R. J., et al. 2014a, ApJ, 786, 134
McCully, C., Jha, S. W., Foley, R. J., et al. 2014b, Natur, 512, 54
Meng, X., & Podsiadlowski, P. 2014, ApJL, 789, L45
Miller, A. A., Kasliwal, M. M., Cao, Y., et al. 2017, ApJ, 848, 59
Miller, A. A., Yao, Y., Bulla, M., et al. 2020, ApJ, 902, 47
Narayan, G., Foley, R. J., Berger, E., et al. 2011, ApJL, 731, L11
Nicholl, M. 2018, RNAAS, 2, 230
Nordin, J., Brinnel, V., van Santen, J., et al. 2019, A&A, 631, A147
Nordin, J., Maguire, K., Miller, A., et al. 2020a, TNSAN 2020-185
Nordin, J., Maguire, K., Miller, A., et al. 2020b, TNSCR 2020-2940
Nordin, J., & Perley, D. 2020, TNSTR 2020-2929
Nugent, P. E., Sullivan, M., Cenko, S. B., et al. 2011, Natur, 480, 344
Phillips, M. M. 1993, ApJL, 413, L105
Phillips, M. M., Li, W., Frieman, J. A., et al. 2007, PASP, 119, 360
Phillips, M. M., Lira, P., Suntzeff, N. B., et al. 1999, AJ, 118, 1766
Riess, A. G., Filippenko, A. V., Li, W., et al. 1999, AJ, 118, 2675
Sahu, D. K., Tanaka, M., Anupama, G. C., et al. 2008, ApJ, 680, 580
Schlafly, E. F., & Finkbeiner, D. P. 2011, ApJ, 737, 103
Seitenzahl, I. R., Ciaraldi-Schoolmann, F., Röpke, F. K., et al. 2013, MNRAS, 429, 1156
Sim, S. A., Seitenzahl, I. R., Kromer, M., et al. 2013, MNRAS, 436, 333
Singh, M., Misra, K., Sahu, D. K., et al. 2018, MNRAS, 474, 2551
Singh, M., Misra, K., Sahu, D. K., et al. 2022, MNRAS, 517, 5617

[27] https://hesma.h-its.org
[28] http://leda.univ-lyon1.fr

Singh, M., Sahu, D. K., Dastidar, R., et al. 2023, ApJ, 953, 93
Sorce, J. G., Tully, R. B., Courtois, H. M., et al. 2014, MNRAS, 444, 527
Spergel, D. N., Bean, R., Doré, O., et al. 2007, ApJS, 170, 377
Srivastav, S., Smartt, S. J., Huber, M. E., et al. 2022, MNRAS, 511, 2708
Srivastav, S., Smartt, S. J., Leloudas, G., et al. 2020, ApJL, 892, L24
Stritzinger, M. D., Hsiao, E., Valenti, S., et al. 2014, A&A, 561, A146
Stritzinger, M. D., Valenti, S., Hoeflich, P., et al. 2015, A&A, 573, A2
Taubenberger, S. 2017, in Handbook of Supernovae, ed. A. W. Alsabti & P. Murdin (Berlin: Springer), 317
Theureau, G., Hanski, M. O., Coudreau, N., Hallet, N., & Martin, J. M. 2007, A&A, 465, 71
Thomas, R. C., Nugent, P. E., & Meza, J. C. 2011, PASP, 123, 237
Tomasella, L., Cappellaro, E., Benetti, S., et al. 2016, MNRAS, 459, 1018
Tomasella, L., Stritzinger, M., Benetti, S., et al. 2020, MNRAS, 496, 1132
Tully, R. B., Courtois, H. M., Dolphin, A. E., et al. 2013, AJ, 146, 86
Tully, R. B., Courtois, H. M., & Sorce, J. G. 2016, AJ, 152, 50
Valenti, S., Benetti, S., Cappellaro, E., et al. 2008, MNRAS, 383, 1485
Valenti, S., Howell, D. A., Stritzinger, M. D., et al. 2016, MNRAS, 459, 3939
Valenti, S., Sand, D., Pastorello, A., et al. 2014, MNRAS, 438, L101
Wang, X., Filippenko, A. V., Ganeshalingam, M., et al. 2009, ApJL, 699, L139
Wang, X., Li, W., Filippenko, A. V., et al. 2008, ApJ, 675, 626
Wang, X., Wang, L., Filippenko, A. V., Zhang, T., & Zhao, X. 2013, Sci, 340, 170
White, C. J., Kasliwal, M. M., Nugent, P. E., et al. 2015, ApJ, 799, 52
Yamanaka, M., Maeda, K., Kawabata, K. S., et al. 2015, ApJ, 806, 191
Yaron, O., & Gal-Yam, A. 2012, PASP, 124, 668